



Article

Inverse Synthetic Aperture Radar Imaging of Space Targets Using Wideband Pseudo-Noise Signals with Low Peak-to-Average Power Ratio

Simon Anger ^{*}, Matthias Jirousek, Stephan Dill and Markus Peichl

German Aerospace Center (DLR), Microwaves and Radar Institute, Muenchenerstrasse 20, 82234 Weßling, Germany; matthias.jirousek@dlr.de (M.J.); stephan.dill@dlr.de (S.D.); markus.peichl@dlr.de (M.P.)

* Correspondence: simon.anger@dlr.de

Abstract: With the number of new satellites increasing dramatically, comprehensive space surveillance is becoming increasingly important. Therefore, high-resolution inverse synthetic aperture radar (ISAR) imaging of satellites can provide an in-situ assessment of the satellites. This paper demonstrates that pseudo-noise signals can also be used for satellite imaging, in addition to classical linear frequency-modulated chirp signals. Pseudo-noise transmission signals offer the advantage of very low cross-correlation values. This, for instance, enables the possibility of a system with multiple channels transmitting instantaneously. Furthermore, it can significantly reduce signal interference with other systems operating in the same frequency spectrum, which is of particular interest for high-bandwidth, high-power systems such as satellite imaging radars. A new routine has been introduced to generate a wideband pseudo-noise signal with a peak-to-average power ratio (PAPR) similar to that of a chirp signal. This is essential for applications where the transmit signal power budget is sharply limited by the high-power amplifier. The paper presents both theoretical descriptions and analysis of the generated pseudo-noise signal as well as the results of an imaging measurement of a real space target using the introduced pseudo-noise signals.

Keywords: inverse synthetic aperture radar (ISAR); noise radar; pseudo noise; radar imaging; space targets; satellites; space surveillance



Citation: Anger, S.; Jirousek, M.; Dill, S.; Peichl, M. Inverse Synthetic Aperture Radar Imaging of Space Targets Using Wideband Pseudo-Noise Signals with Low Peak-to-Average Power Ratio. *Remote Sens.* **2024**, *16*, 1809. <https://doi.org/10.3390/rs16101809>

Academic Editors: Cyril Grima and Vassilis Karamanavis

Received: 28 March 2024

Revised: 7 May 2024

Accepted: 10 May 2024

Published: 20 May 2024



Copyright: © 2024 by the authors. Licensee MDPI, Basel, Switzerland. This article is an open access article distributed under the terms and conditions of the Creative Commons Attribution (CC BY) license (<https://creativecommons.org/licenses/by/4.0/>).

1. Introduction

Imaging radars widely use linear frequency-modulated chirp signals to provide broadband characteristics and gather fine range resolution. Chirp signals have an inherently low peak-to-average power ratio (PAPR), which enables power-efficient long-range radar imaging with limited peak transmit power. This is achieved by using a matched filter for range compression, which maximizes the signal-to-noise ratio (SNR). Linear frequency modulations can be either increasing (up-chirp) or decreasing (down-chirp), while non-linear frequency modulations include exponential or hyperbolic modulations [1,2]. In noise radar technology (NRT), random waveforms are transmitted instead of the classical, often sophisticated, deterministic radar signals [3–6]. Compared to deterministic signals, the non-deterministic nature of noise-like transmitted signals can provide advantages in radar imaging. Noise signals and their spread spectrum properties can reduce mutual interference with other radars and communication systems operating in the same frequency spectrum. Due to their low cross-correlation values and quasi-orthogonality, it would be possible to operate several transmitters simultaneously using different noise signals [7,8]. Another well-known advantage is the Low Probability of Intercept (LPI) of noise-like signals, which reduces their visibility to electronic support measures (ESM) and electronic intelligence systems (ELINT). They are more resistant to interference and adversarial attacks such as jamming and signal exploitation (LPE) [9–11].

Nowadays, it is possible to generate analog transmit signals with a random characteristic using an arbitrary waveform generator (AWG). The AWG is capable of converting a digitally available arbitrary signal characteristic into an analog transmit signal using a sample rate of several giga samples per second (GS/s) and analog bandwidths of up to several GHz. The actual characteristic of the signal can be generated by means of software algorithms. The electronics available today allow the receiver to sample the signal with an analog-to-digital converter (ADC) at up to several GS/s with a subsequent fully digital signal processing, enabling comprehensive signal calibrations and error corrections for arbitrary signals used. A digitally matched filter can be used to perform range compression and maximize the SNR. Just like with deterministic signals, the achievable range resolution depends not on the time domain signal characteristic but is determined by the signal bandwidth or, more precisely, the spectral shape of the noise signal [10,12,13].

The German Aerospace Center (DLR) operates an experimental satellite imaging radar called IoSiS (Imaging of Satellites in Space) using a high degree of digital technology able to generate arbitrary transmit signals [14,15]. IoSiS contains a pulse radar system working around the X band with an instantaneous bandwidth of up to 4.4 GHz [16,17]. In the transmitter, a traveling-wave tube amplifier (TWTA) is used to generate the high output pulse power. Due to the limited output peak power of amplifiers, the pulse transmit signal should exhibit a low peak-to-average power ratio (PAPR). This achieves the TWTA's maximum achievable average power, ultimately resulting in a good SNR in the radar image [11]. Especially in the field of space surveillance, tracking or imaging radars, where small targets or low radar cross sections (RCS) have to be tracked or imaged, efficient utilization of the available power is of crucial importance. Hence, using a Gaussian noise signal with its high PAPR as a transmit signal leads to a loss of SNR. A special pseudo-noise signal is required that has the signal characteristics of a noise signal together with a low PAPR like a chirp signal. In addition, LPI and LPE properties as well as the quasi-orthogonality must be retained. This paper outlines the iterative process for creating a pseudo-noise signal with the aforementioned properties. It also includes the theoretical analysis of the signal and its generation based on the IoSiS system parameters for experimental verification measurements. One focus is on investigating the experimental results and the signal's applicability with IoSiS components. Finally, an ISAR measurement of the International Space Station (ISS) using IoSiS is described to demonstrate that the pseudo-noise signal is capable of high-resolution phase-coherent imaging.

2. Pseudo-Noise Signals as Transmit Signal

In radar remote sensing, the power budget of the radar system is critical for achieving a sufficient signal-to-noise ratio (SNR) in the measurement results when detecting or imaging small targets with low radar cross sections (RCS). Therefore, a crucial requirement is to maximize the energy of the transmitted radar signal. With pulse radar technology and a given duration of the transmit pulse, an increase in the energy of the radar pulse can only be achieved by increasing the average power of the pulse. Together with the fact that every high power amplifier (HPA) that supplies the power for the transmit signal has a certain saturation point at which the maximum output power is limited, it results in that the ratio between the average pulse power and the peak pulse power should be as small as possible to maximize the SNR. The PAPR of any time discrete signal characteristic $s(n)$ of length N can be calculated as follows:

$$PAPR = \frac{\max |s(n)|^2}{\frac{1}{N} \sum_{n=1}^N |s(n)|^2} = \left(\frac{|\hat{s}|}{s_{RMS}} \right)^2 \quad (1)$$

In any case, where the average power is less than the peak power of the signal, this will result in a loss of SNR, which can be calculated as follows:

$$SNR_{loss} = -10 \log_{10}(PAPR) \quad (2)$$

If we consider as an example a real-valued frequency modulated chirp signal with a peak amplitude of \hat{s} , and further $s_{RMS} = \hat{s} / \sqrt{2}$ the root mean square (RMS) of a sinusoidal signal, the PAPR can be calculated with $\hat{s}^2 / s_{RMS}^2 = 2$. Chirp signals with their low PAPR can drive the HPA around its saturation point without changing the signal characteristic in its correlation behavior due to clipping or nonlinearity effects and hence constitute a very power-efficient signal. The main objective of the present work was to generate and experimentally validate a pseudo-noise signal (PNS) that has a comparable power efficiency to a chirp signal, while retaining its fundamental noise characteristics, such as the spread-spectrum properties, LPI, and low cross-correlation values. In the next section, the generation procedure and the basic signal characteristics of the pseudo-noise signal are described.

2.1. Generation Procedure of Pseudo-Noise Signal

With regard to the experimental verification measurements with the IoSiS radar system, the design of the PNS focused on the basic system parameters of IoSiS. These parameters included a system bandwidth of 2.8 GHz, a pulse duration of about 40 μ s, and a signal sampling rate of 10 GS/s. Furthermore, the signal should have a peak-to-peak amplitude of $u_{pp} = 2$ V, corresponding to an average power of 10 dBm considering a chirp like PAPR. In addition, in view of the experimental measurement for which the signals are to be designed, only real-valued signals are considered in the following.

The iterative generation procedure is shown in Figure 1. The initial signal used here is a Gaussian noise signal $s_N(t)$ with a standard deviation significantly larger than the intended signal amplitude of the PNS. It should hold $\sigma(s_N(t)) > a \cdot u_{pp}$ with $a > 1000$. In two steps, the signal is shaped. First, in the time domain, the peak amplitude is limited by clipping at u_{pp} . Therefore, the values greater than u_p or less than $-u_p$ will be set to u_p or $-u_p$, respectively. Secondly, with $S(f) = \mathfrak{F}(s(t))$, the signal is shaped in the frequency domain to the intended bandwidth characteristic $H_{BP}(f)$. In the following work, $H_{BP}(f)$ equals a rectangular function. By repeating these shaping steps a minimum of 15 times, a PNS signal with a chirp-like PAPR will be generated.

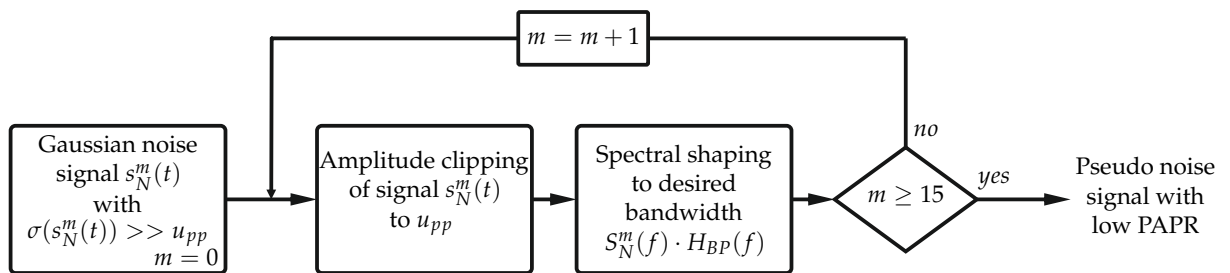


Figure 1. Iterative generation of an amplitude and bandwidth-limited pseudo-noise signal with a low peak-to-average power ratio (PAPR). The generated pseudo-noise signal is limited to the peak-to-peak amplitude u_{pp} in the time domain and to the transfer function $H_{BP}(f)$ in the frequency domain.

The time domain signal of the generated PNS together with a Gaussian noise and a classical chirp signal is shown in Figure 2. In addition, the probability density function (PDF) of the amplitude in the time domain is depicted. All signals shown have an average pulse power of 10 dBm considering an impedance of 50 Ω . Furthermore, the signals exhibit a bandwidth of 2.8 GHz with the cutoff frequencies 200 MHz and 3 GHz. The Gaussian noise signal can be described with the PDF as follows:

$$F_{PDF}(a) = \frac{1}{\sqrt{2\pi\sigma^2}} \exp\left(-\frac{a^2}{2\sigma^2}\right) \tag{3}$$

with the variance of the signal of length $t_2 - t_1$:

$$\sigma^2 = \frac{1}{t_2 - t_1} \int_{t_1}^{t_2} s^2(t) dt \quad (4)$$

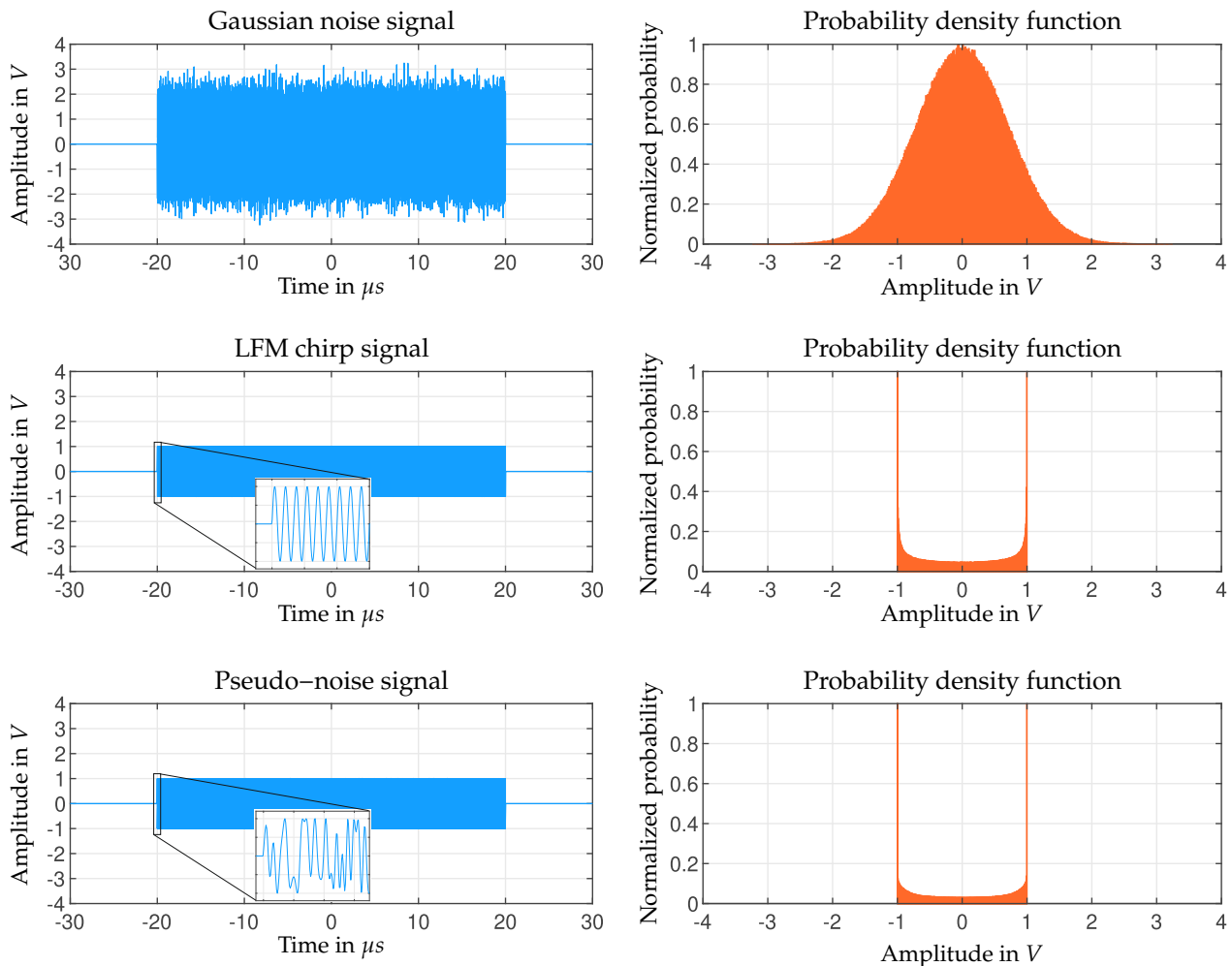


Figure 2. Three different pulse signals with the same average power of 10 dBm. A Gaussian noise signal with the variance $\sigma^2 = 0.5$ V and the corresponding probability density function (PDF) of the time domain amplitude values. A classical linear frequency modulated chirp signal and the corresponding PDF. A sharp amplitude limited pseudo-noise signal generated with the procedure described in Figure 1 and the corresponding PDF.

Further, for the normalized power of a time-continuous random signal or the ergodic process, we can write [18]:

$$P_N = \lim_{T \rightarrow \infty} \frac{1}{2T} \int_{-T}^T s^2(t) dt \quad (5)$$

In the case where the linear time average of the signal is zero, we can see by comparing (4) and (5) that $\sigma^2 \equiv P_N$ [19]. Consequently, the variance of the signal is the normalized (reference impedance 1 Ω) power of our Gaussian signal. With the intended average signal power of 10 dBm and an impedance of 50 Ω, this results in a variance of $\sigma^2 = 0.5$ V and a standard deviation of $\sigma = 0.707$ V (Figure 2 (top)). The time domain signal and the PDF show that a significant number of values up to around 3 V appear in a Gaussian noise

signal with an average power of 10 dBm. Hence, the signal exhibits a high PAPR of about 34 compared to the chirp signal with a PAPR of 2. A chirp signal, however, has a sharp limited amplitude in the time domain (Figure 2 (center)). Considering an average signal power of 10 dBm, the chirp signal exhibits a peak amplitude of 1 V. This also applies to the PNS generated, as described before (Figure 2 (bottom)). Furthermore, the PDFs from chirp and PNS exhibit strikingly similar behavior. This is not immediately apparent when only the enlarged section of the two signals is compared. However, when the entire length of the signal is considered, the majority of the amplitude values fall within the range of approximately 1 or -1 volt, which gives rise to this distinctive PDF. Given that the chirp signal and the PNS signal exhibit a comparable PNS, it follows that the average power and, consequently, the PAPR of both signals are identical.

2.2. Short-Time Fourier Analysis

To analyze the spread-spectrum properties of the PNS, the results of a short-time Fourier transformation (STFT) are shown in Figure 3. The LFM chirp signal shows its typical characteristic where the signal energy is focused at a small instantaneous bandwidth. The PNS signal, however, has a characteristic very similar to that of the Gaussian noise and, as a result, it also exhibits as Gaussian noise a large instantaneous bandwidth [20], indicating a proper LPI. The spread-spectrum properties are a distinct advantage in the reduction in interference with systems that share the same frequency spectrum. Especially when very high pulse powers are used in combination with very large transmission bandwidths, appropriate interference mitigation is essential.

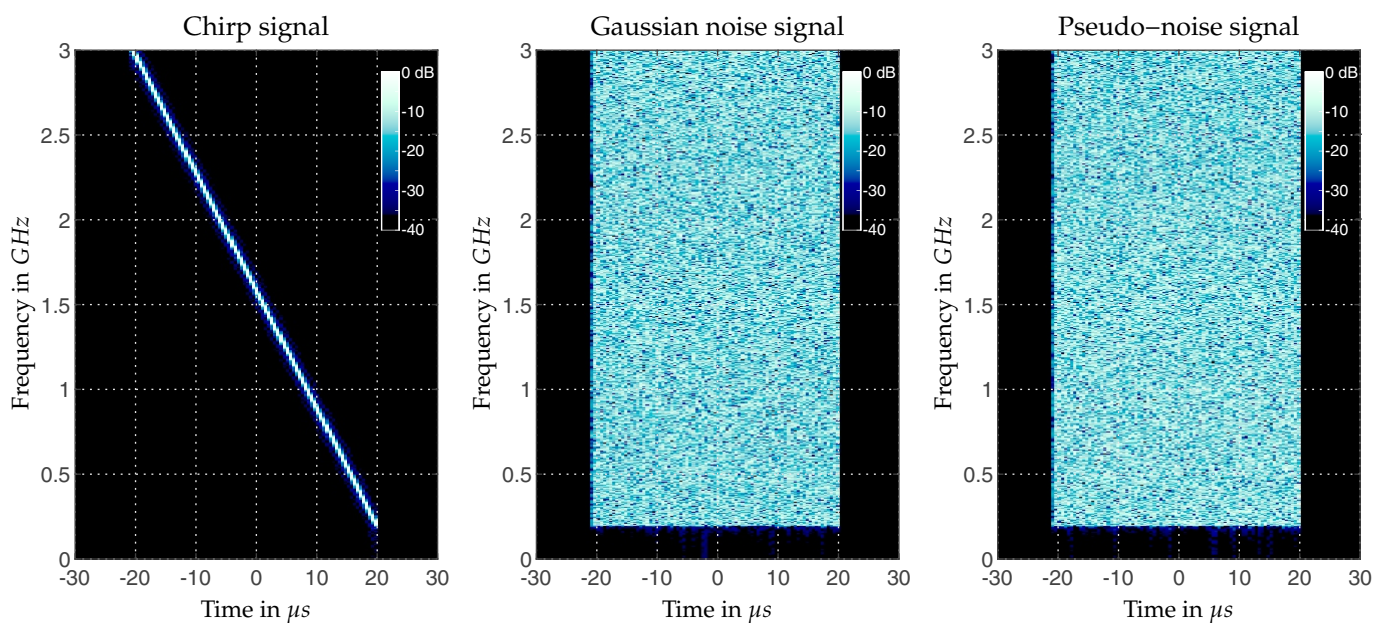


Figure 3. Short-time Fourier transform (STFT) of a chirp, Gaussian noise, and the generated pseudo-noise signal. The STFT indicates that the pseudo-noise signal exhibits very similar characteristics to a Gaussian noise signal.

2.3. Point Spread Function and Cross-Correlation Analyses

A key feature when using the PNS signal as a radar transmit signal is an appropriate autocorrelation function (ACF). The ACF defines the range profile of an ideal, frequency-independent point target, neglecting noise, attenuation, and distortion. When using a chirp signal with bandwidth B and a rectangular envelope in the frequency domain, the power representation of the range profile of a single point target ideally corresponds to a $\text{sinc}(x)^2/x^2$ function, showing a typical suppression of the first side lobe level of about 13.3 dB. Further, with c the speed of light, the first zero of the sinc-function can be calculated

with c/B and the half-power beam width (HPBW) corresponds to $0.89 \cdot (c/2B)$, representing the range resolution of the radar [2].

In radar systems, a matched filter approach represents the correlation between the transmit signal $s_t(t)$ and the conjugated, time-reversed version of the received signal $s_r(t)$. This convolution is often carried out in the frequency domain due to the lower computational effort. With $\mathfrak{F}(\cdot)$ the Discrete Fourier Transform (DFT) and $S_t(f) = \mathfrak{F}(s_t)$ and $S_r(f) = \mathfrak{F}(s_r)$, we obtain the following matched filter output:

$$s_{mf}(t) = \mathfrak{F}^{-1}\left(S_t(f) \circ S_r^*(f)\right) \quad (6)$$

where \circ denotes the point-wise multiplication (Hadamard product). In the ideal case, $s_r(t)$ equals $s_t(t - \Delta t)$. If we further neglect the time shift Δt between the transmit and receive signal, the output of the matched filter represents the ACF defined by:

$$s_{ACF}(\tau) = \int_{-\infty}^{\infty} s(t)s^*(t - \tau) dt \quad -\infty < \tau < \infty \quad (7)$$

Figure 4 shows the ACF of a Gaussian noise signal in comparison with the ACF of the PNS. Both signals have a bandwidth of 2.8 GHz, an initial pulse duration of 40 μ s and a rectangular envelope in the frequency domain. Both show a nearly ideal characteristic down to an amplitude below -35 dB and a suppression of the first side lobe of 13.3 dB. The zeros between the side lobes have a slightly higher amplitude in the PNS case. However, in the practical case of experimental measurements, this small deviation can be neglected. The HPBW of about 54 mm corresponds to the theoretical value.

In addition, the cross-correlation function (CCF) between two different Gaussian and PNS pairs is shown in Figure 4. Again, both cross-correlated signals have a bandwidth of 2.8 GHz, a rectangular frequency envelope, a pulse duration of 40 μ s, and a rectangular envelope in the frequency domain. With respect to the peak amplitude, the CCF values are mostly below -50 dBc for both signal types. The result shows that the generated PNSs are also well-suited for multiple access applications in NRT [21].

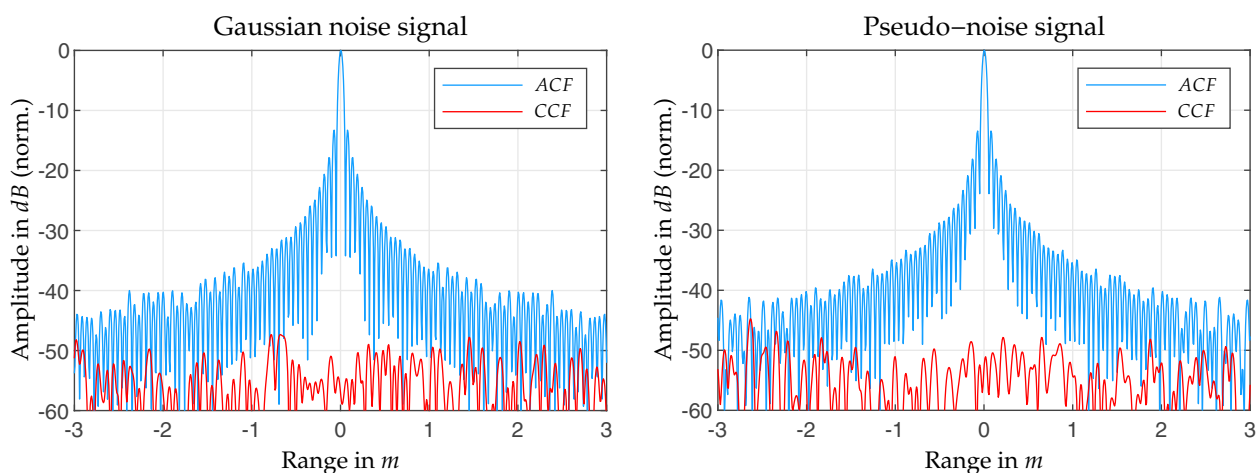


Figure 4. Simulated point spread functions using a Gaussian noise as well as the pseudo-noise signal (PNS) with a signal bandwidth of 2.8 GHz. Both exhibit a nearly ideal characteristic down to an amplitude below -35 dB. Similar to the Gaussian noise signal, a pair of PNSs exhibits very low cross-correlation (CCF) values, indicating its quasi-orthogonality.

To demonstrate the beneficial impact of a more expansive signal bandwidth, Figure 5 illustrates the ACF and CCF with half and double bandwidth compared to the characteristics shown in Figure 4. The larger bandwidth has a positive influence on the ACF as well as the CCF. In the case of a signal bandwidth of 5.6 GHz, the attenuation of the side lobes

increases faster corresponding to the finer range resolution. The CCF also shows lower values when broadband signal characteristics are used.

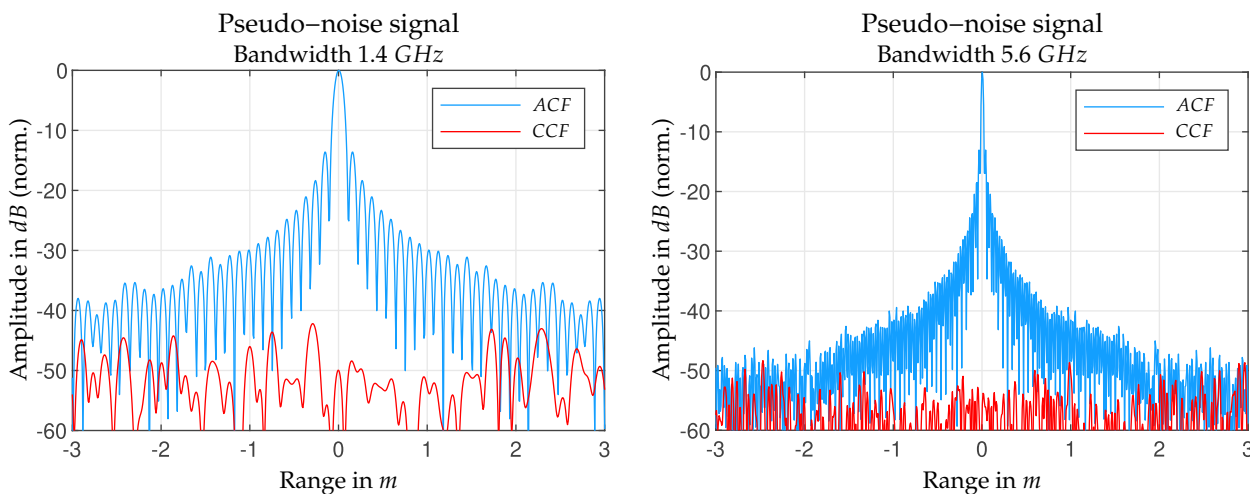


Figure 5. Simulated point spread functions using the PNS with different signal bandwidths.

2.4. Ambiguity Function

The ambiguity function illustrates the sensitivity of the PSF regarding a shift in time or frequency, respectively. In the signal processing of pulsed radar, an ambiguity function is a two-dimensional function of the propagation delay Δt and the Doppler shift frequency f_D . For a given complex base band pulse $s(t)$, the narrow band ambiguity function is given by [1,22]:

$$\chi(\Delta t, f_D) = \int_{-\infty}^{\infty} s(t)s^*(t - \Delta t)e^{i2\pi f_D t} dt \tag{8}$$

For broadband signals, the Doppler shift, represented in (8) by $e^{i2\pi f_D t}$, can no longer be assumed to be constant with respect to the instantaneous frequency within a broadband pulse signal. The movement of the target causes the wide-band signal to expand or compress in time. This effect can no longer be approximated by a simple frequency “shift”. Therefore the wideband ambiguity function (WBA) was introduced [23–26]:

$$\chi_{wb}(\Delta t, v_r) = \sqrt{|\alpha|} \int_{-\infty}^{\infty} s(t)s^*(\alpha(t - \Delta t)) dt \quad \text{with} \quad \alpha = \frac{c + v_r}{c - v_r} \tag{9}$$

Here, V is the radial target velocity with respect to the radar and c is the speed of light.

The simulated WBA of an LFM chirp signal and a generated PNS is shown in Figure 6 for two different pulse duration’s τ_{pulse} and a bandwidth of 2.8 GHz. Satellites in a low Earth orbit travel with an orbital velocity of about 7.6 km/s, with the result that very high radial velocities can occur during the imaging process [27,28]. The radial velocities of $v_r = \pm 1$ km/s, used for the simulation, hence are typical values in space target imaging; however, they can be even higher at very low elevation angles of the antenna, pointing towards the space target during the pass.

In contrast to the chirp signal, stochastic signals are very sensitive to frequency shifts caused by a Doppler frequency. This also applies to the PNS signal, which can be recognized by the rapid decrease in amplitude with increasing $|v_r|$. The longer the pulse duration, the more sensitively the PNS reacts to a Doppler shift. A longer pulse duration leads to an increase in time compression or expansion of the Doppler effect, and hence, the negative effect of the radial velocity component increases significantly.

The WBA of an LFM chirp signal shows a temporal shift with increasing $|v_r|$, which can also be expressed as a shift along the range direction. At higher $|v_r|$, there is a defocusing

effect which becomes more pronounced as the pulse duration becomes longer due to an increase in time compression or expansion, respectively.

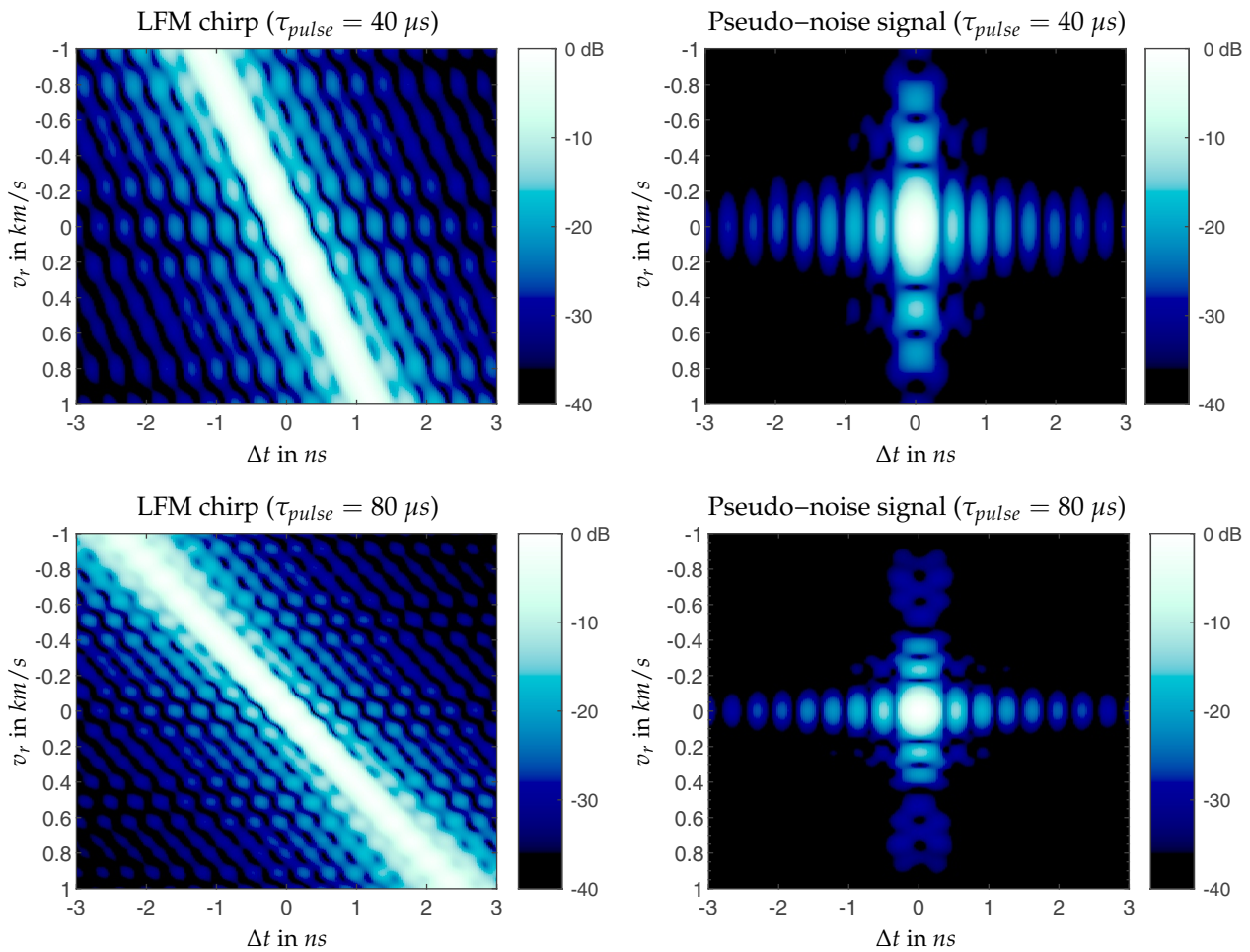


Figure 6. Wideband ambiguity function of a linear frequency modulated (LFM) chirp signal (left) and a generated pseudo-noise (right) for typical radial velocities v_r as they occur in radar-based imaging of satellites.

When considering the PNS, the Doppler sensitivity must be taken into account, and an appropriate mitigation procedure must be applied to avoid severe loss of SNR. In the case of space target imaging, v_r can be properly determined and its degradation effect mitigated because the trajectory and spatial velocity vectors of the target are well known [28].

2.5. Spectral Kurtosis

Spectral kurtosis (SK) can be used to analyze the PNS for its stationary characteristics and to quantify its LPI properties [5]. SK is a statistical tool that can indicate and locate non-stationary or non-Gaussian behavior in the frequency domain. A stationary time series has statistical properties or moments, for example, mean and variance, that do not vary in time. A small value of SK for a frequency bin indicates the existence of stationary Gaussian noise, whereas a high positive value indicates the existence of a transient or structured signal at the corresponding frequency [29,30]. The SK of a signal $S(f_k)$ can be calculated with:

$$SK(f) = \frac{\sum_{k=b_1}^{b_2} (f_k - C_1)^4 S(f_k)}{(C_2)^4 \sum_{k=b_1}^{b_2} S(f_k)} \quad (10)$$

with C_1 the spectral centroid:

$$C_1(f) = \frac{\sum_{k=b_1}^{b_2} f_k S(f_k)}{\sum_{k=b_1}^{b_2} S(f_k)} \quad (11)$$

and C_2 the spectral spread:

$$C_2(f) = \sqrt{\frac{\sum_{k=b_1}^{b_2} (f_k - C_1)^2 S(f_k)}{\sum_{k=b_1}^{b_2} S(f_k)}} \quad (12)$$

here b_1 and b_2 are the band edges in bins of the frequency spectrum under investigation. f_k is the frequency in Hz, and $S(f_k)$ is the signal value of the k^{th} bin, respectively [31].

The SK of a Gaussian noise signal and the PNS are shown in Figure 7. The section of the baseband signal spectrum being investigated, ranging from 200 MHz to 3 GHz, is highlighted. Both signals exhibit low SK values and thus show their stationary characteristics. This shows that the iteratively generated PNS still contains its stationary characteristic and an LPI. By way of comparison, the SK values of a chirp signal are in the region of 100, which is indicative of its deterministic, non-stationary nature.

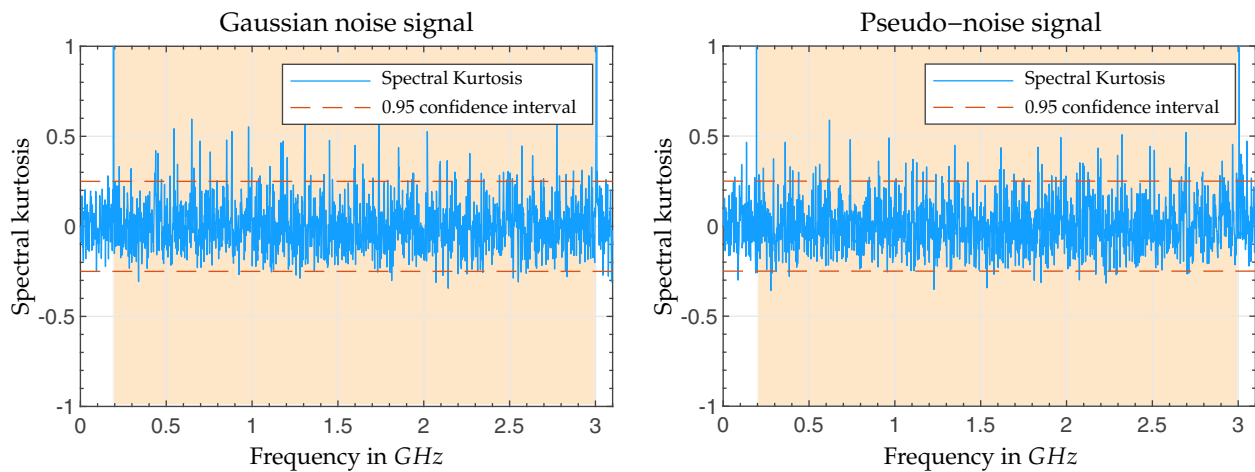


Figure 7. Comparison of the Spektral Kurtosis (SK) of Gaussian noise and the generated pseudo-noise signal. The orange highlighted section shows the frequency range of the signal from 200 MHz to 3 GHz. The low SK values of the pseudo-noise signal show its stationary signal behavior and hence its low LPI properties.

3. Experimental Verification Measurements

For the experimental verification measurements of the generated PNS, the IoSiS radar system is used [14]. The first step is to investigate whether the radar can obtain high-resolution range profiles by using the PNS. This is performed using an internal calibration path measurement. The space target used is the ISS (International Space Station), which is a well-known target and has been imaged several times with IoSiS using chirp signals [32].

3.1. IoSiS System Description

IoSiS is an experimental satellite imaging radar using pulse radar techniques and working around the X band. Figure 8 shows the hardware setup containing a multi-dish-based steerable antenna system, a TWTA (white box behind the main reflector), and a container for the main radar electronics. The main 9 m dish antenna is used as the transmitting antenna

and two 1.8 m antennas are used for receiving. In the results presented in the following, only one receive antenna, i.e., one receive channel, has been used. The radar electronics enable fully digital signal generation and acquisition across the entire simultaneous radar bandwidth. In the current mode, IoSiS achieves a maximum simultaneous bandwidth of 2.8 GHz with an RF center frequency of 10.2 GHz. This corresponds to the lower sideband (LSB) considering a local oscillator (LO) frequency of 11 GHz.

Figure 9 shows the RF schematic of the transmit and one receive path. Isolators, amplifiers, and attenuators have been partially omitted for the sake of simplicity. In the transmit path, the AWG enables the digital-to-analog conversion of the generated PNS with a sample rate of 10 GS/s in the baseband. After the up-conversion into the RF band, bandpass filters work as image rejection filters, where the LSB filter is used in the measurement results presented. The TWTA at a short distance from the feed network of the Cassegrain antenna ensures the required high pulse power. A common LO source ensures coherent up- and down-conversion in the transmit and receive path, which is a prerequisite for the application of ISAR imaging techniques. In the receive path, a low-noise amplifier (LNA) ensures an appropriate receiver noise temperature. Bandpass filters in turn ensure a proper image rejection, and after down-conversion, a digital-to-analog converter samples the signal in the time domain at a sampling rate of up to 10 GS/s.

For calibration, in which the system's transfer function is corrected, a calibration path is provided that diverts an attenuated version of the transmit signal directly into the receive path. In this work, the calibration path is used to check the system behavior when using the PNS as a transmission signal before a real imaging measurement is performed.



Figure 8. A photo of the IoSiS setup is shown, featuring a 9 m transmitting antenna in a Cassegrain configuration and two 1.8 m receiving antennas. The radar electronics responsible for signal generation and acquisition are housed in a nearby container.

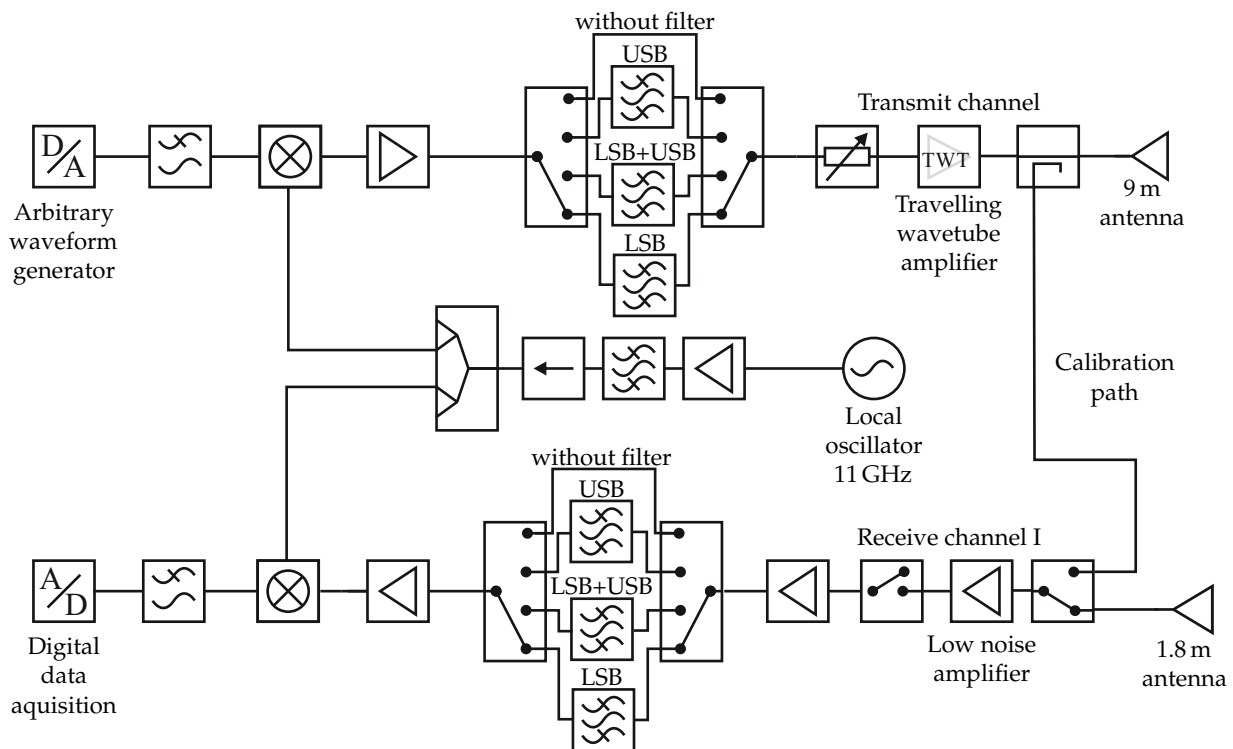


Figure 9. Simplified RF diagram of the IoSiS radar, showing the transmit channel and one of the two receive channels. Fully digital signal generation and acquisition enables the generation of arbitrary transmit signals. Filter banks in each channel enable operation in the upper (USB) and lower side band (LSB).

3.2. Point Spread Function Analysis Measurements

Essential for high-resolution ISAR imaging is a focused point spread function (PSF) together with the coherence, i.e., phase stability over time. When considering the PNS as a transmit signal, the behavior of the TWTA is of particular interest. A TWTA is operated at or even in saturation. Therefore, distortion and harmonics may be introduced into the amplified signal due to non-linearity between the input and output signals, which can degrade the PSF. The PNS, with its spread spectrum characteristics, provides the TWTA with an input signal that delivers the full system bandwidth at the same time. Therefore, in combination with the non-linear characteristic of the TWTA and in contrast to a chirp signal, which has a low instantaneous bandwidth, harmonics and intermodulation distortions can occur.

In the following, the calibration path (see Figure 9) is used to determine the PSF when using the PNS. For this, the first step is to perform a calibration of the system for the correction of a non-ideal transfer function (TF). A chirp signal is used to determine the TF and to generate a calibration signal to compensate for frequency-dependent characteristics (non-constant group delay) and amplitude variations of radar system components such as amplifiers and filters. The detailed calibration procedure can be found in [16,17].

The measured PSF using the PNS is shown in Figure 10 with a rectangular (unweighted) spectrum and a Hamming weighting. The measurement parameters are listed in Table 1. The non-ideal transfer function of the radar system, including the dispersion characteristics and the time shift caused by the propagation delay of the radar system components, is already compensated by using the calibration signal mentioned above. In the unweighted case, the PSF represents the expected sinc-function with an HPBW of 54 mm, corresponding to the bandwidth used, and the first side lobes are around -13.3 dBc. As can already be seen in the simulation results (see Figure 4), the side lobes below -35 dBc show a slight fluctuation of the amplitude.

Also shown is the CCF of a pair of PNS signals, both measured using the calibration path. As in the simulation results, the CCF values are mostly below -50 dBc with respect to the ACF where signal power is maximized. This demonstrates that the quasi-orthogonality is not significantly affected by the system.

Coherence analysis is performed by evaluating the phase of the range profiles at the point of maximum signal power (peak). The phase values of the 2000 range profiles are displayed in Figure 11, along with the phase PDF. The phase values exhibit a Gaussian distribution with a standard deviation of merely 0.3 degrees. This extremely small range of values is not expected to have any negative effects on the experimental measurements. It confirms the phase stability of the system, along with the PNS.

The results of the PSF analysis demonstrate that high-resolution range profiles can be achieved using the PNS together with the IoSiS system. Furthermore, the coherence of the measurements is guaranteed. The following section presents the measurement results of a space target using the PNS as the transmit signal.

Table 1. Measurement parameter for the determination of the PSF using the PNS.

Parameter	Symbol	Parameter Value	Unit
Signal type	-	PNS	-
Center frequency	f_c	10.2	GHz
Bandwidth	B	2.8	GHz
Range resolution	Δr	54	mm
DAC sampling rate	f_{DAC}	10	GS/s
ADC sampling rate	f_{ADC}	10	GS/s
Pulse duration	τ_{pulse}	45	μ s
PRF	prf	200	Hz
Signal type	-	PNS	-
Mode	-	LSB	-

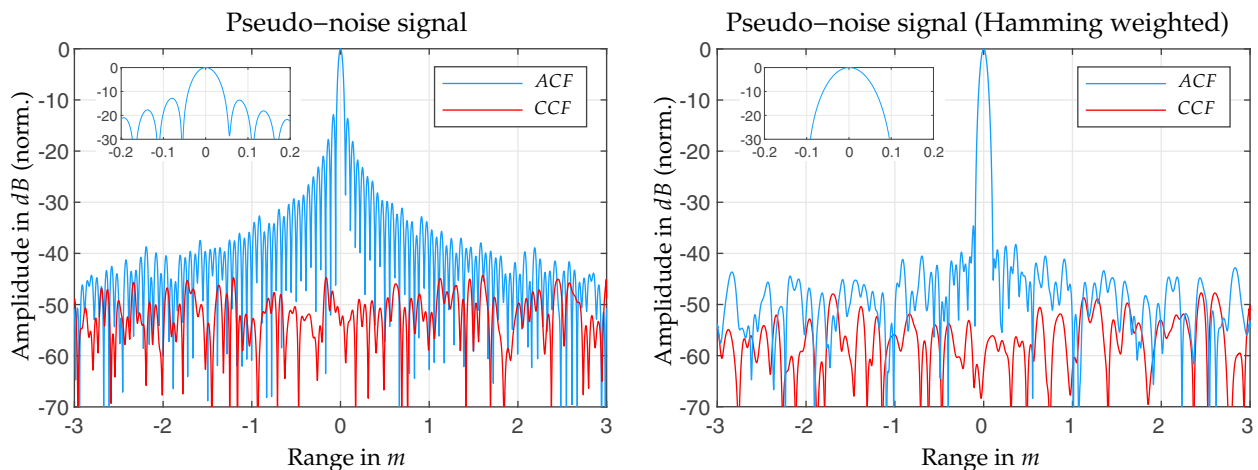


Figure 10. Measured point spread function (PSF) using the pseudo-noise signal routed through the calibration path of the radar system (**left**). Spectral weighted PSF of the pseudo-noise signal (**right**). In the non-weighted case, the half-power beam width (HPBW) corresponds to the applied pulse signal bandwidth of 2.8 GHz and equals about 54 mm. In both cases, the low cross-correlation (CCF) values show the quasi-orthogonality of a pair of pseudo-noise signals.

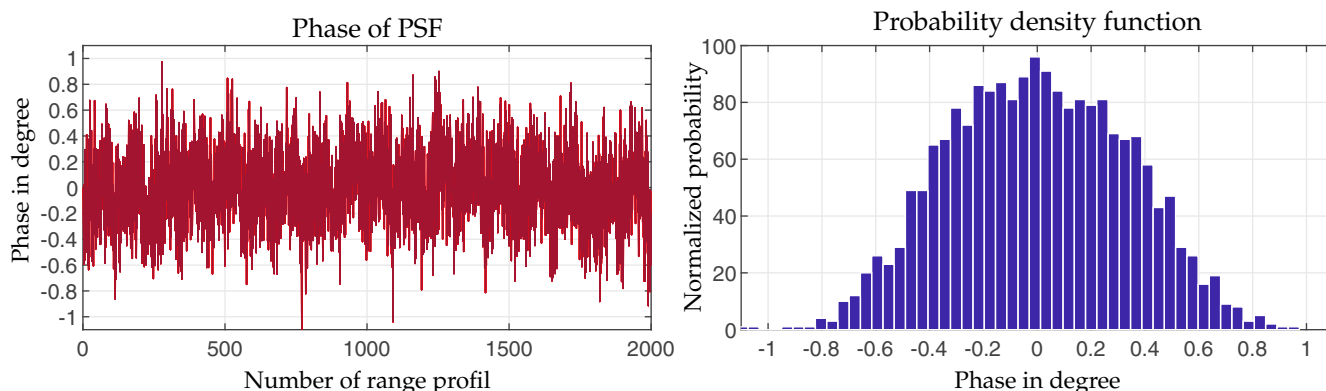


Figure 11. Phase values extracted in the maximum amplitude of the ACF point spread function (PSF) measured using the calibration path of the IoSiS radar (left). Corresponding phase probability function (PDF) of the measured phase values (right). With a phase standard deviation of $\sigma = 0.3^\circ$, the phase is highly stable, which is a prerequisite for using the PNS in an ISAR system.

3.3. ISAR Space Target Measurement Results

An ISAR measurement of the ISS is performed using IoSiS to verify the PNS in a real space target measurement. The same PNS is used here for the PSF verification measurements described in the previous section. The same calibration steps were applied to achieve high spatial resolution as in measurements with a chirp signal. This includes antenna calibration and calibration of the radar system transfer function. A detailed description of the processing steps can be found in [14].

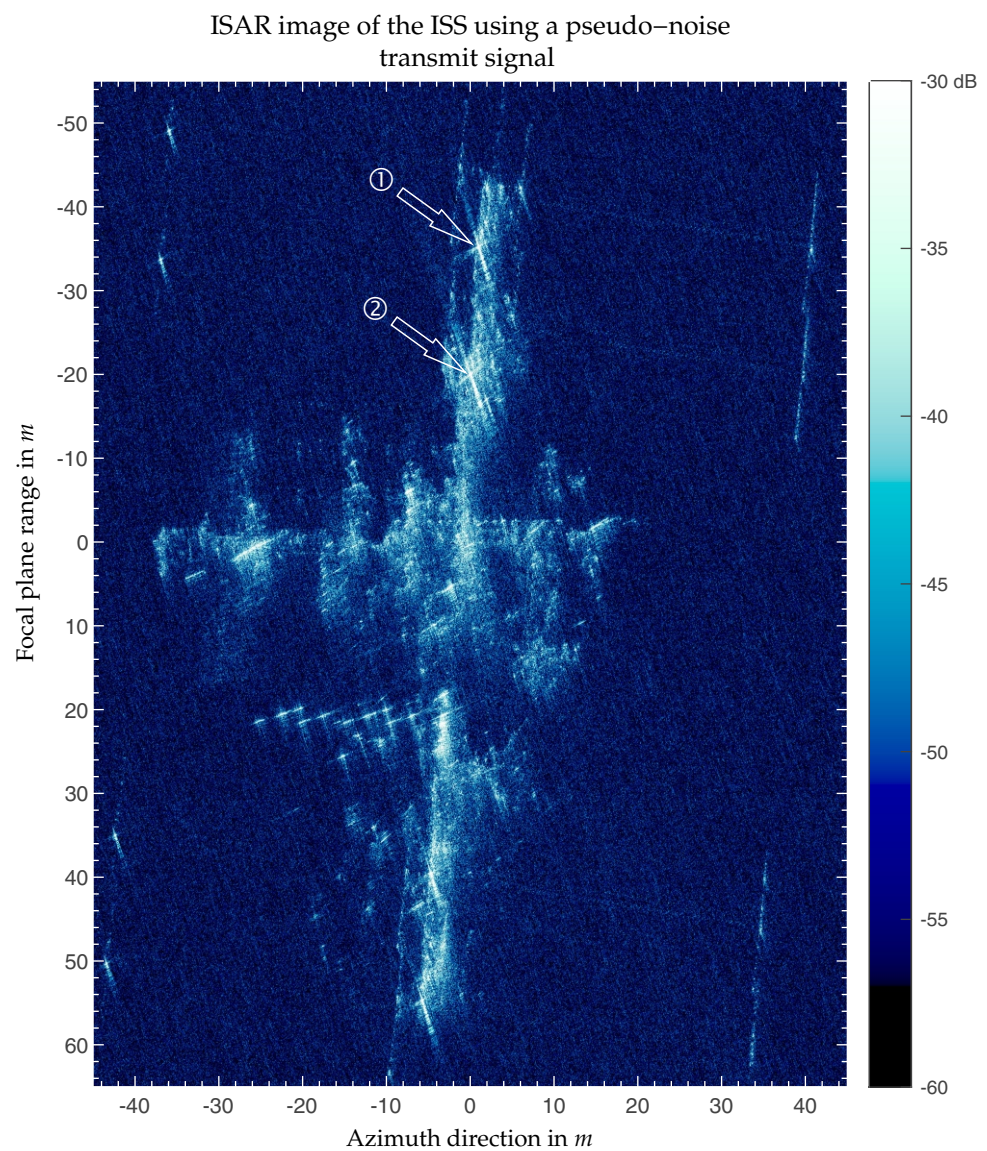
The measurement parameters and the resulting theoretical image parameters are shown in Table 2. The theoretical slant range and azimuth resolution are 54 mm and 53 mm respectively, corresponding to the signal bandwidth and azimuth integration angle [32]. As the focal plane, used for the back-projection of the range profiles, was chosen according to the spatial orientation of the ISS, we have to consider the degradation of the range resolution based on the focal plane incident angle θ_{FP} . With the slant range resolution Δr , the FP resolution is $\Delta r_{FP} = \Delta r \cdot \cos(\theta_{FP})^{-1}$. The actual spatial resolution of the FP is therefore between 67 mm and 74 mm, taking into account the changes in the angle of incidence during the measurement.

The final ISAR imaging result, after completing all processing steps is depicted in Figure 12. The image shows great detail of the entire ISS with high backscatter along the vertically aligned main truss segment as well as along the horizontally aligned various modules. The grid structures between the individual solar arrays are slightly visible, as is the end of the solar arrays with their characteristic RCS. The planar solar panels themselves are not visible. They are rotated on a continuous basis so that they are aligned with the sun. For this reason, they can only be seen if the time of day of the measurement and the imaging geometry match.

To provide an objective assessment of the spatial resolution achieved and to evaluate the PNS signal employed, two robust scatterers are analyzed in depth. The positions of these scatterers under investigation are indicated with arrows in the ISAR image. Both are located either on or in close proximity to the FP, ensuring an undisturbed PSF. These scatterers near the main truss segment have been observed in various measurements of the ISS and exhibit a wide-angle backscatter behavior that allows for comprehensive, fundamental radar verification. The distance between the scatterers is approximately 15 m, which enables examination of the focus over a wide area. However, it is important to note that these structures are not ideal isolated calibration targets as they are surrounded by other components. There are several radar calibration spheres orbiting the earth, but they cannot be used with the IoSiS system due to their high altitude together with its low RCS [33].

Table 2. Measurement parameter for the ISAR image shown in Figure 12 using the PNS .

Parameter	Symbol	Parameter Value	Unit
Transmit signal type	-	PNS	-
Center frequency	f_c	10.2	GHz
Bandwidth	B	2.8	GHz
Integration angle	ϕ_{Az}	16	degree
Slant range resolution	Δr	54	mm
Azimuth resolution	Δr_{Az}	53	mm
FP incident angle	θ_{FP}	36.2–43	degree
FP range resolution	Δr_{FP}	67–74	mm
DAC sampling rate	f_{DAC}	10	GS/s
ADC sampling rate	f_{ADC}	10	GS/s
Pulse duration	τ_{pulse}	45	μ s
PRF	prf	190	Hz
Target distance	r_t	600–680	km
Processed pulses	N_{pulses}	5000	km
Processing algorithm	-	Back-projection	-
Image size	-	6000 \times 9000	Pixel
Mode	-	LSB	-

**Figure 12.** ISAR image of the ISS using a PNS transmit signal together with the IoSiS radar system. The achieved spatial resolution in range and azimuth direction was evaluated by analyzing two robust scatterers. The arrows indicate the positions of the scatterers under investigation.

Both sections of the ISAR image containing the robust scatterers are depicted in Figure 13. The amplitude of each image is normalized based on its own maximum to independently extract the characteristics of the PSF. The image is accompanied by the cuts in the FP range and azimuth directions for each PSF. It is obvious that there are interfering structures in the second PSF at the bottom left of the main lobe area that could affect the robustness of the analyzed target. But the cuts still show that a decent resolution could be achieved. The resolution values around 70 mm are within expectation in the FP range (refer to Table 2). In the azimuth direction, both PSFs exhibit a slightly worse resolution compared to the theoretical value. This indicates that there may be minor residual errors that have not been mitigated or non-idealities of the target.

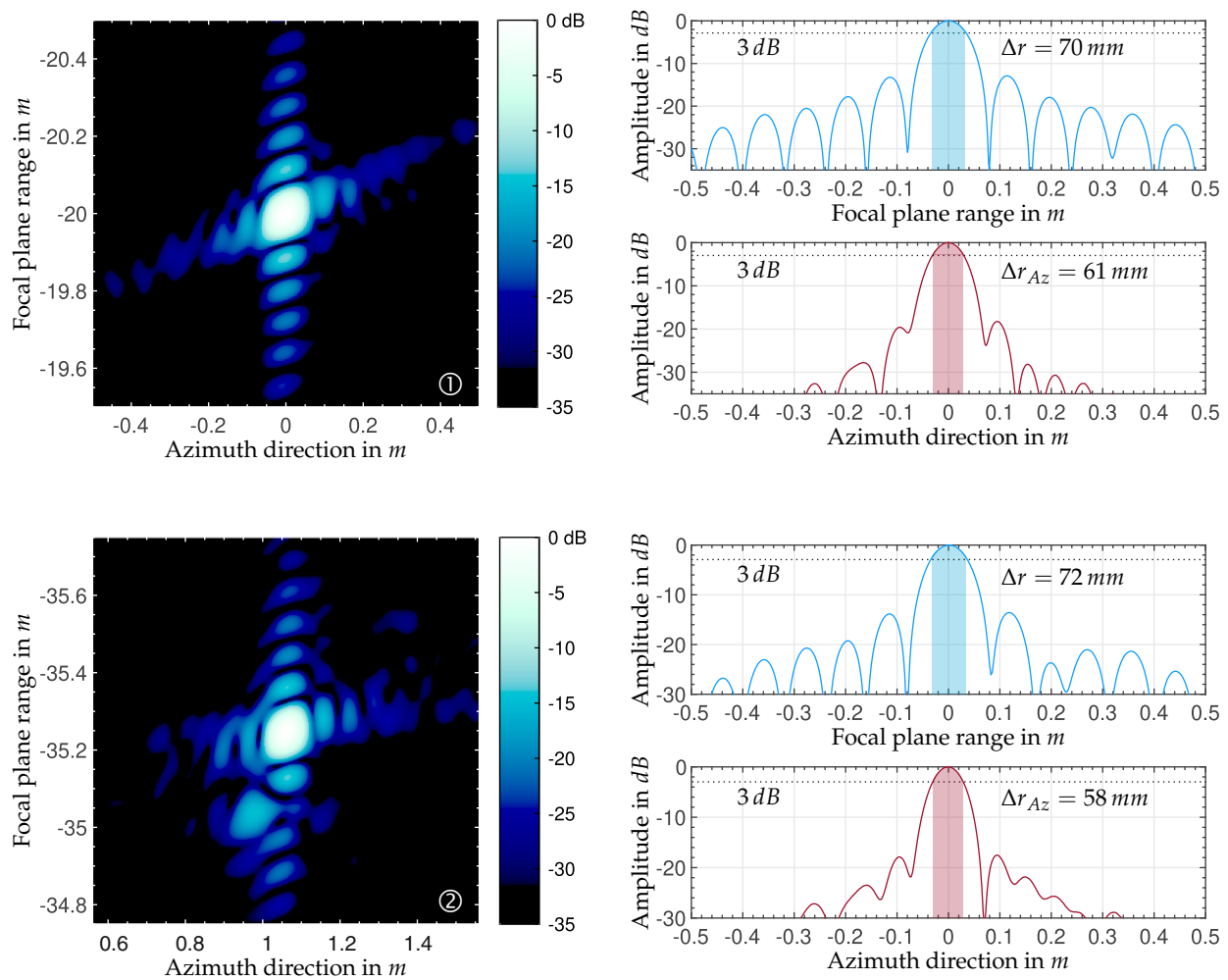


Figure 13. ISAR image of the isolated robust scatterers of the ISS, together with the cuts in the cardinal direction, to analyze the PSF and to evaluate the PNS signal used. The HPBW in the focal plane (Δr) of both are in the expected range. In the azimuth direction, both exhibit a slightly higher HPBW (Δr_{Az}) considering the integration angle.

The suppression of the range side lobes is almost ideal, although the second PSF shows some deviations, which are certainly caused by the aforementioned surrounding structure. In azimuth, the ISAR images of both PSFs clearly show that the sidelobes are not perfectly aligned with the azimuth direction. Hence, the cuts of azimuthal side lobes should be viewed with caution as the cuts do not pass through the maximum amplitude of each side lobe. The slanted side lobes are due to the imaging geometry combined with the very large integration angle and projection onto the FP.

In summary, however, the results demonstrate accurate focusing in both spatial directions of two widely separated scatterers, confirming the effectiveness of using a PNS for imaging space targets.

4. Conclusions

This paper describes the investigation of pseudo-noise signals that can be used in particular in ground-based high-resolution ISAR satellite imagery. The non-deterministic nature of noise-like transmission signals can have advantages over deterministic signals. Noise signals and their spread spectrum characteristics can, for example, reduce the mutual interference with other radar systems and communication systems that are operating in the same frequency spectrum.

The studies presented are carried out from the perspective of experimental measurements with the IoSiS satellite imaging radar. The parameters of the IoSiS system were therefore the basis for the investigations. When considering noise signals, the peak-to-average power ratio (PAPR) in particular has been a key point of optimization. A routine is introduced that iteratively generates a pseudo-noise signal (PNS) that has a chirp-like PAPR. In addition to a low PAPR, the aim was to maintain noise characteristics such as spread spectrum, low probability of intercept, and low cross-correlation values. In the presented work, simulation results show that the general properties of stationary noise are still valid for the iteratively generated PNS. Short-term Fourier transformation, ambiguity function, and spectral kurtosis of the PNS were analyzed and evaluated. The simulation results are compared to either Gaussian noise or chirp signals, demonstrating that the PNS still has all the intended characteristics of a stationary noise signal. Experiments using the IoSiS radar system are presented to verify the theoretical results. The first step of the experimental test was the verification of the applicability of the PNS with the IoSiS hardware setup via the calibration path. The analysis of the point spread function (PSF), together with the phase analysis, demonstrates that it is possible to achieve highly resolved range profiles with highly coherent phase behavior using the PNS. Furthermore, the measurement results validate the low cross-correlation values. The potential of the PNS in satellite imaging is demonstrated by performing an ISAR measurement of the ISS.

Author Contributions: S.A.: Conceptualization, data curation, formal analysis, investigation, software, validation, visualization, and writing—original draft. M.J.: Data curation, investigation, writing—original draft, and writing—review and editing. S.D.: Conceptualization, investigation, validation, writing—original draft, and writing—review and editing. M.P.: Conceptualization, funding acquisition, project administration, supervision, and writing—review and editing. All authors have read and agreed to the published version of the manuscript.

Funding: This work has been partially supported by the Federal Office of Bundeswehr Equipment, Information Technology and In-Service Support.

Data Availability Statement: The data that support the findings of this research are partly available from the corresponding author upon reasonable request. The data are not publicly available due to privacy restrictions.

Conflicts of Interest: The authors declare no conflicts of interest.

Abbreviations

The following abbreviations are used in this manuscript:

ACF	Auto correlation function
ADC	Analog-to-digital converter
AF	Ambiguity function
AWG	Arbitrary waveform generator
CCF	Cross-correlation function
DAC	Digital-to-analog converter
ELINT	Electronic intelligence systems

ESM	Electronic support measures
HPA	High power amplifier
HPBW	Half-power beam width
IoSiS	Imaging of satellites in space
ISS	International Space Station
LFM	Linear frequency modulated
LNA	Low noise amplifier
LO	Local oscillator
LPE	Low probability of exploitation
LPI	Low probability of intercept
LSB	Lower side band
NRT	Noise radar technology
PAPR	Peak-to-average power ratio
PDF	Probability density function
PNS	Pseudo-noise signal
PSF	Point spread function
RCS	Radar cross section
RMS	Root mean square
SK	Spectral Kurtosis
SNR	Signal-to-noise ration
STFT	Short-time Fourier transformation
TF	Transfer function
TWTA	Travelling waveltube amplifier
USB	Upper side band
WBA	Wideband ambiguity function

References

- Levanon, N.; Mozeson, E. *Radar Signals*; John Wiley & Sons, Ltd.: Hoboken, NJ, USA, 2004; Chapter 4, pp. 53–73. [\[CrossRef\]](#)
- Skolnik, M. *Introduction to Radar Systems*; Electrical Engineering Series; McGraw-Hill: New York, NY, USA, 2001.
- Palo, F.D.; Galati, G.; Pavan, G.; Wasserzier, C.; Savci, K. Introduction to Noise Radar and Its Waveforms. *Sensors* **2020**, *20*, 5187. [\[CrossRef\]](#) [\[PubMed\]](#)
- Galati, G.; Pavan, G.; De Palo, F.; Stove, A. Potential applications of noise radar technology and related waveform diversity. In Proceedings of the 17th International Radar Symposium (IRS), Krakow, Poland, 10–12 May 2016; pp. 1–5. [\[CrossRef\]](#)
- Savci, K.; Galati, G.; Pavan, G. Low-PAPR Waveforms with Shaped Spectrum for Enhanced Low Probability of Intercept Noise Radars. *Remote Sens.* **2021**, *13*, 2372. [\[CrossRef\]](#)
- Galati, G.; Pavan, G.; Savci, K.; Wasserzier, C. Noise Radar Technology: Waveforms Design and Field Trials. *Sensors* **2021**, *21*, 3216. [\[CrossRef\]](#) [\[PubMed\]](#)
- De Palo, F.; Galati, G. Orthogonal waveforms for multiradar and MIMO radar using noise radar technology. In Proceedings of the Signal Processing Symposium (SPSymo), Debe, Poland, 10–12 June 2015; pp. 1–4. [\[CrossRef\]](#)
- Galati, G.; Pavan, G. Noise Radar Technology as an Interference Prevention Method. *J. Electr. Comput. Eng.* **2013**, *2013*, 146986. [\[CrossRef\]](#)
- De Martino, A. *Introduction to Modern EW Systems*; Artech House: London, UK, 2018.
- Kulpa, K. *Signal Processing in Noise Waveform Radar*; Artech House: London, UK, 2013.
- Galati, G.; Pavan, G.; Savci, K.; Wasserzier, C. Counter-Interception and Counter-Exploitation Features of Noise Radar Technology. *Remote Sens.* **2021**, *13*, 4509. [\[CrossRef\]](#)
- Kulpa, K.; Lukin, K.; Miceli, W.; Thayaparan, T. Signal processing in noise radar technology. *IET Radar Sonar Navig.* **2008**, *2*, 229–323. [\[CrossRef\]](#)
- Narayanan, R.M.; Xu, X. Principles and applications of coherent random noise radar technology. *Noise Devices Circuits* **2003**, *5113*, 503–514. [\[CrossRef\]](#)
- Anger, S.; Jirousek, M.; Dill, S.; Kempf, T.; Peichl, M. High-resolution inverse synthetic aperture radar imaging of satellites in space. *IET Radar Sonar Navig.* **2023**, *18*, 544–563. [\[CrossRef\]](#)
- Anger, S.; Jirousek, M.; Dill, S.; Peichl, M. Imaging of objects in space using arbitrary transmit signals. In Proceedings of the 14th European Conference on Synthetic Aperture Radar, Leipzig, Germany, 25–27 July 2022; pp. 1–5.
- Jirousek, M.; Iff, S.; Anger, S.; Peichl, M. GigaRad—A multi-purpose high-resolution ground-based radar system concept, error correction strategies and performance verification. *Int. J. Microw. Wirel. Technol.* **2015**, *7*, 443–451. [\[CrossRef\]](#)
- Jirousek, M.; Dill, S.; Schreiber, E.; Anger, S.; Peichl, M.; Schreiber, H. Characteristics of the high-performance highly digitized multi-purpose radar system GigaRad: System Concept, System Correction and Calibration, Applications. In Proceedings of the 2018 11th German Microwave Conference (GeMiC), Freiburg, Germany, 12–14 March 2018; pp. 395–398. [\[CrossRef\]](#)
- Lindner, J. *Informationsübertragung*; Springer-Lehrbuch; Springer: Berlin/Heidelberg, Germany, 2005.

19. Ohm, J.R.; Lüke, H.D. *Signalübertragung Grundlagen der Digitalen und Analogen Nachrichtenübertragungssysteme*, 11th ed.; Springer: Berlin/Heidelberg, Germany; New York, NY, USA, 2010. [\[CrossRef\]](#)
20. Boashash, B. Estimating and interpreting the instantaneous frequency of a signal. I. Fundamentals. *Proc. IEEE* **1992**, *80*, 520–538. [\[CrossRef\]](#)
21. Ipatov, V. *Spread Spectrum and CDMA: Principles and Applications*; Wiley: West Sussex, UK, 2005.
22. Balleri, A.; Farina, A. Ambiguity function and accuracy of the hyperbolic chirp: Comparison with the linear chirp. *IET Radar Sonar Navig.* **2017**, *11*, 142–153. [\[CrossRef\]](#)
23. Dawood, M.; Narayanan, R. Generalised wideband ambiguity function of a coherent ultrawideband random noise radar. *IEE Proc. Radar Sonar Navig.* **2003**, *150*, 379. [\[CrossRef\]](#)
24. Sune, R.A. Generalized Ambiguity Functions for Ultra Wide Band Random Waveforms. In Proceedings of the International Radar Symposium, Krakow, Poland, 24–26 May 2006; pp. 1–4. [\[CrossRef\]](#)
25. Sibul, L.; Ziomek, L. Generalized wideband crossambiguity function. *IEEE Int. Conf. Acoust. Speech Signal Process.* **1981**, *6*, 1239–1242. [\[CrossRef\]](#)
26. Sen, S.; Nehorai, A. Adaptive Design of OFDM Radar Signal With Improved Wideband Ambiguity Function. *IEEE Trans. Signal Process.* **2010**, *58*, 928–933. [\[CrossRef\]](#)
27. Anger, S.; Jirousek, M.; Dill, S.; Schreiber, E.; Peichl, M. Imaging of satellites in space (IoSiS): Challenges in image processing of ground-based high-resolution ISAR data. In *Proceedings of the Radar Sensor Technology XXII*; Ranney, K.L., Doerry, A., Eds.; International Society for Optics and Photonics, SPIE: Bellingham, WA, USA, 2018; Volume 10633, p. 106330L. [\[CrossRef\]](#)
28. Montenbruck, O.; Gill, E. *Satellite Orbits: Models, Methods, and Applications*; Physics and Astronomy Online Library; Springer: Berlin/Heidelberg, Germany, 2000.
29. Antoni, J. The spectral kurtosis: A useful tool for characterising non-stationary signals. *Mech. Syst. Signal Process.* **2006**, *20*, 282–307. [\[CrossRef\]](#)
30. Antoni, J.; Randall, R. The spectral kurtosis: Application to the vibratory surveillance and diagnostics of rotating machines. *Mech. Syst. Signal Process.* **2006**, *20*, 308–331. [\[CrossRef\]](#)
31. Peeters, G. *A Large Set of Audio Features for Sound Description (Similarity and Classification) in the CUIDADO Project*; Technical Report; Ircam: Paris, Paris, 2004.
32. Anger, S.; Jirousek, M.; Dill, S.; Peichl, M. ISAR imaging of space objects using large observation angles. In Proceedings of the 21st International Radar Symposium (IRS), Berlin, Germany, 21–22 June 2021.
33. McDowell, J. Navel Research Laboratory Satellites 1960–1989. *J. Br. Interplanet. Soc.* **1997**, *50*, 427–432.

Disclaimer/Publisher’s Note: The statements, opinions and data contained in all publications are solely those of the individual author(s) and contributor(s) and not of MDPI and/or the editor(s). MDPI and/or the editor(s) disclaim responsibility for any injury to people or property resulting from any ideas, methods, instructions or products referred to in the content.